Template synthesis of two-dimensional ternary nickel-cobalt-nitrogen co-doped porous carbon Þlm: Promoting the conductivity and more active sites for oxygen reduction

Mancai Qian [a,b], Meijiao Xu [a], Shuqing Zhou [a], Jianniao Tian [a], Tayirjan Taylor Isimjan [c], Zhongfeng Shi [b], Xiulin Yang [a]

[a] Guangxi Key Laboratory of Low Carbon Energy Materials, School of Chemistry and Pharmaceutical Sciences, Guangxi Normal University, Guilin 541004, People's Republic of China
[b] College of Chemistry and Chemical Engineering, Qinzhou University, Qinzhou 535000, People's Republic of China
[c] Saudi Arabia Basic Industries Corporation (SABIC) at King Abdullah University of Science and Technology (KAUST), Saudi Arabia

highlights

- Ternary Ni/Co/N co-doped porous carbon Þlm (Ni-Co-N@CF) is fabricated by a simple controllable and scalable strategy.
- The Ni-Co-N@CF catalyst exhibits a large electrochemically active surface area and maximum diffusion limited current density.
- The catalyst demonstrates a superior anti-poisoning capacity and long-term stability.
- The excellent ORR activities are attributed to the synergetic interactions of ternary doping of Ni/Co/N in the Þlm skeleton.
- The ternary Ni/Co/N in the Þlm can enhance electron conductivity and provide more Co-N active sites.

graphical abstract

article info

Article history:
Received 12 October 2019
Revised 17 December 2019
Accepted 20 December 2019
Available online 20 December 2019

Keywords:
Ternary doping
2D porous carbon Þlm
Oxygen reduction reaction
Synergistic interaction
Electrocatalysts

abstract

Rational design of a stable, highly active non-precious metal-based electrocatalysts for oxygen reduction reaction (ORR) is vitally important for industrial application of fuel cells technology. As a potential alternative of Pt/C catalyst, two-dimensional (2D) porous carbon materials are widely investigated due to the highly accessible surface area and active sites, wherein carbon Þlms doped with a plurality of metals and non-metal elements are rarely reported due to an uncontrollable synthesis process. Here, a bi-metallic

doping of Ni/Co/N in the 2D film skeleton, which not only greatly enhances conductivity but also provides more Co-N active sites.

1. Introduction

Oxygen reduction reaction (ORR) is one of the cornerstone reactions for energy conversion and storage devices, such as fuel cells, metal-air batteries [1,2]. However, the commercialization of these devices has been hindered due to the sluggish reaction kinetics that require high over-potential to drive ORR and performance deterioration at the cathode. Platinum (Pt) and platinum-based materials have been recognized as state-of-the-art electrocatalysts for ORR because of a direct four-electron oxygen reduction within a relatively low overpotential [3,4]. Nevertheless, the high cost, limited reserves, and poor durability are key obstacles for its broad application in fuel cells, metal-air batteries, and industrialization [5,6]. Great endeavors have been focused on developing non-precious metal materials as cost-effective, efficient and durable ORR electrocatalysts [7–9].

Amongst these explorations, the nitrogen-doped two-dimensional (2D) carbon materials have recognized as the emerging ORR electrocatalysts since it has large surface area, high active site density, and the excellent electrical conductivity [10]. In addition, C—N composites supported Ni or Co could further improve the electrocatalytic performance due to the change of electronegativity of carbon substrate [11–13]. To date, the synthesis methods of 2D carbon materials include chemical vapor deposition (CVD) method and template assisted pyrolysis organic substances [14–17]. However, the above strategies require suitable template or structural directing agent or repeated calcinations/leaching process, which lead to complex synthesis process, time-consuming and difficult to scale up [18,19]. Therefore, besides the overcoming technical challenge, designing a simple synthesis process that is suitable for industrial application is the crucial step for the commercialization of ORR cathode technology. To our best knowledge, very few reports of bimetallic catalysts, especially Ni/Co particles, toward ORR could be found so far [20–22]. Moreover, the catalytic activity and stability of the catalysts need to be further improved compared with Pt/C. Given these, developing a simple strategy that allows cost-effective and scalable preparation of nitrogen-doped 2D carbons supported Ni/Co bimetallic catalyst is necessary.

Herein, we report a sodium chloride template assisted and scalable approach towards synthesis of Ni/Co/N ternary elements co-doped porous carbon film as ORR catalysts by direct pyrolysis of biomolecule guanine aggregates, NaCl, and $NiCo_2O_4$. The catalyst, labeled as Ni-Co-N@CF, exhibits highly catalytic activity, excellent durability, and superior methanol tolerance towards ORR in alkaline solution. The electrochemical test result of control sample has confirmed that the metallic NiCo alloy nanoparticles and Co-N active sites played a crucial role in enhancing the ORR activity. The synergetic interactions from the metallic Ni/Co particles, 2D -doped carbon film and Co-N active sites are ascribe to account for the excellent ORR activity comparable to commercial 20 wt% Pt/C.

2. Experimental section

All chemical reagents are analytical grade and used without further purification. The NiCo LDH was prepared by the previously reported method with minor modifications [23]. In a typical synthesis, 2.5 mmol $Ni(NO_3)_2·6H_2O$ and 4 mmol $Co(NO_3)_2·6H_2O$ were dissolved in a mixture solvent of 37.5 mL ethylene glycol and 12.5 mL deionized water. Then, 37.5 mmol of urea was added under magnetic stirring. The resulting solution was transferred into in a round-bottom flask to be refluxed under vigorous magnetic stirring for 3 h at 90 °C. The precipitates were collected by centrifugation and washed several times with distilled water until the residual solution was colorless, and then frozen and freeze-dried at □52 °C in a vacuum lyophilizer for overnight.

The $NiCo_2O_4$ material was obtained by calcination of NiCo-LDH in a ceramic crucible at 350 °C for 2 h with a heating rate of 2 °C $min^{□1}$ in air.

For the synthesis of Ni-Co-N@CF, 5.0 g sodium chloride was ultrasonically dissolved in 10 mL deionized water. After that 2.0 g guanine and 25 mg $NiCo_2O_4$ were added into the above solution and stirred for 0.5 h until getting a gray seriflux. Until the solvent was evaporated at 80 °C, the collected powders were grinded in a quartz mortar and then subjected to carbonizing at different temperatures (800–1100 °C) for 2 h with a heating rate of 5 °C $min^{□1}$ under N_2 atmosphere. The resulting black powder was subsequently washed with abundant deionized water to remove sodium chloride, then ethanol for twice and finally dried at 60 °C. The products are termed as Ni-Co-N@CF (X) (X = 800, 900, 1000 and 1100 °C). If not specified, the Ni-Co-N@CF discussed in the work refers to the Ni-Co-N@CF (900 °C).

As a comparison, the products using different mass of $NiCo_2O_4$ (15 and 50 mg) were further explored and denoted as Ni-Co-N@CF-15 and Ni-Co-N@CF-50, respectively. Moreover, the control samples, including Ni-N@CF, Co-N@CF and N@CF, were synthesized by the similar strategy as discussed above.

The working electrode was polished with 0.05 μm alumina powder and rinsed with water, 0.5 M H_2SO_4 and ethanol for 3 times, respectively. The catalyst inks were prepared by ultrasonically dispersing the catalyst (4 mg) in 1.0 mL mixed solvent with 490 μL isopropanol, 495 μL deionized water and 10 μL of 5 wt% Nafion. Then, 19.6 μL of inks were pipetted onto the surface of glassy carbon electrode (ϕ = 5.61 mm) and naturally dried for use. The loading of all catalysts was calculated as 0.318 mg $cm^{□2}$ except that the loading of commercial Pt/C (20 wt% Pt, JM) was 0.081 mg $cm^{□2}$.

A rotating ring-disk electrode (RRDE) of 5.61 mm in diameter separately modified by different catalysts was served as working electrode in O_2-saturated 0.1 M KOH. The kinetic parameters, kinetic current densities, hydrogen peroxide yields and electron transfer numbers for ORR were calculated and discussed in detail in supporting experimental section.

The LSV curves and chronoamperometric responses of the prepared catalysts and commercial Pt/C (20 wt% Pt) were recorded on an electrochemical workstation (Pine Research Instrumentation,

Inc., Durham, NC, USA) with a conventional three-electrode cell. The Ag/AgCl (sat. KCl) and a graphite plate are used as reference and counter electrode, respectively. All the potentials values were calibrated with respect to the reversible hydrogen electrode (RHE) of E(RHE) = E(Ag/AgCl) + 0.96 V (Fig. S1).

The ORR activity of these catalysts was evaluated in O_2- or N_2-saturated 0.1 M KOH solution at a scan rate of 10 mV $s^{□1}$ with varying rotating speeds from 400 to 2025 rpm. The methanol crossover effects in CVs for Ni-Co-N@CF and Pt/C were recorded by adding 3.0 M methanol into the O_2-saturated 0.1 M KOH. The methanol poisoning measurements also recorded by chronoamperometric response in O_2-saturated KOH solution at a rotation speed of 1600 rpm with adding 3.0 M methanol at 200 s. The stability tests were carried out by chronoamperometric technique at a rotation rate of 1600 rpm in O_2-saturated electrolyte for 35000 s.

3. Results and discussion

The ternary Ni/Co/N co-doped 2D porous carbon film (Ni-Co-N@CF) was prepared by a controllable three steps (Scheme 1). In the first step, the ethylene glycol molecule forms a coordination precursor with different metal cations (Ni^{2+}/Co^{2+}), and is gradually converted into NiCo-LDH film-like structure under the alkaline environment created by urea hydrolysis [23]. After calcination in air, a stable $NiCo_2O_4$ material is prepared. In the second step, the guanine molecules are uniformly and fully adsorbed on the surface of $NiCo_2O_4$ with the aid of saturated NaCl solution. After drying, the $NiCo_2O_4$/guanine/NaCl mixed powder was obtained. In the third step, the dried mixed powder was placed in a tube furnace and carbonized at different temperatures under Ar atmosphere. After a large amount of H_2O/ethanol washing, a series of porous Ni-Co-N@CF composites were prepared. In contrast, the Ni-N@CF, Co-N@CF, and N@CF were also prepared using the similar approach as discussed above.

The phase and crystal structures of the synthesized products were first examined via X-ray diffraction (XRD) and the results were shown in Fig. 1a. Three sharp peaks at 44.3°, 51.6°, and 76.4° of Ni-N@CF sample in Fig. 1a matched well with the (1 1 1), (2 0 0), and (2 2 0) crystal planes of the face-centered cubic Ni (Ni, JCPDS: 01-1258), respectively [24,25], confirming that NiO in the precursor is effectively reduced to Ni metal nanoparticles. Moreover, the corresponding characteristic diffraction peaks of Ni-Co-N@CF are located in between those of Co (Co JCPDS: 15-0806) and Ni (Ni JCPDS: 01-1258), indicating the formation of alloyed NiCo nanoparticles (Fig. S2) [26]. The broad peak around 26° can be index to the graphitic carbon [27,28]. No typical peaks of cobalt/nickel oxides can be detected, suggesting that the oxide contents are very low or exist in an amorphous form. As shown in Fig. S3a, the diffraction peaks of NiCo-LDH centered at 11.5°, 20.9°, 35.2° and 61.5° that can be assigned to the (0 0 3), (0 0 3), (0 1 2) and (1 1 3) planes of nickel cobalt carbonate hydroxide hydrate (JCPDS: 40-0216) [29]. In addition, the as-prepared Co $(OH)_2$ and $Ni(OH)_2$ materials were in good agreement with previous reported results [23]. Fig. S3b-d show the typical diffraction peaks of Co_3O_4, NiO and $NiCo_2O_4$ obtained from Co-LDH, Ni-LDH and NiCo-LDH after annealed at 350 °C for 2 h in air, respectively. To clarify the $NiCo_2O_4$ sample from NiCo LDH only contain the $NiCo_2O_4$ phase, we carefully compared the XRD patterns of $NiCo_2O_4$ with the mixture of Co_3O_4 and NiO (molar ratio of 1.25:2) and NiCo oxide from different n(Ni^{2+}): n(Co^{2+}) in the precursor. From the XRD results in Fig. S4a, we find that the two characteristic peaks of $NiCo_2O_4$ at 44.6° and 64.8° are different from those of the physical mixture of Co_3O_4 and NiO where the pure Co_3O_4 and NiO show the corresponding typical peaks at 44.9° & 65.3° and 43.3° & 62.9° respectively. While the more Co^{2+} in the precursor, the peaks of corresponding oxide shift to a high degree, indicating the formation of Co oxide (Co_3O_4). The peaks of the NiCo oxide shift to a low degree when the more Ni^{2+} in the precursor, suggesting the formation of NiO (Fig. S4b).

The morphologies of the as-prepared samples were further characterized by scanning electron microscopy (SEM) and transmission electron microscopy (TEM). The SEM image shows that NiCo-LDH exhibits a rugae-like nanofilm morphology (Fig. 1b). After calcination, no visual change in morphology was detected (Fig. 1c). The ultra-thin film structure of Ni-Co-N@CF composite was subsequently confirmed by TEM image (Fig. 1d), where the Ni-Co-N@CF consists of abundant semitransparency film with wrinkled edges. The high-resolution TEM shows that the NiCo alloy nanoparticles has a single crystal structure with a lattice spacing of 0.21 nm, corresponding to the (1 1 1) crystal plane of NiCo alloy nanoparticles (Fig. 1e). The average particle size of the metallic nanoparticles is 1.3 nm, as shown in the TEM (Fig. S5). Additionally, the HAADF-STEM and corresponding elemental mappings revealed that the elements of C, N, Ni and Co were uniformly distributed on the entire architectures of Ni-Co-N@CF (Fig. 1f).

Raman spectroscopy is an efficient method for discerning the disorder and graphitic structures of carbon materials. As shown in Figs. 2a and S6, the Raman spectra of all samples display two

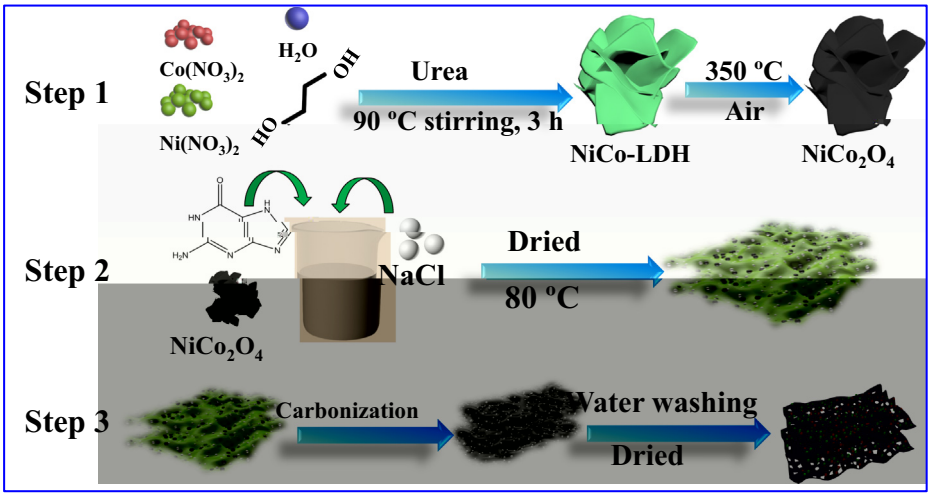

Scheme 1. Schematic diagram of the preparation process of ternary Ni/Co/N co-doped 2D porous carbon film (Ni-Co-N@CF).

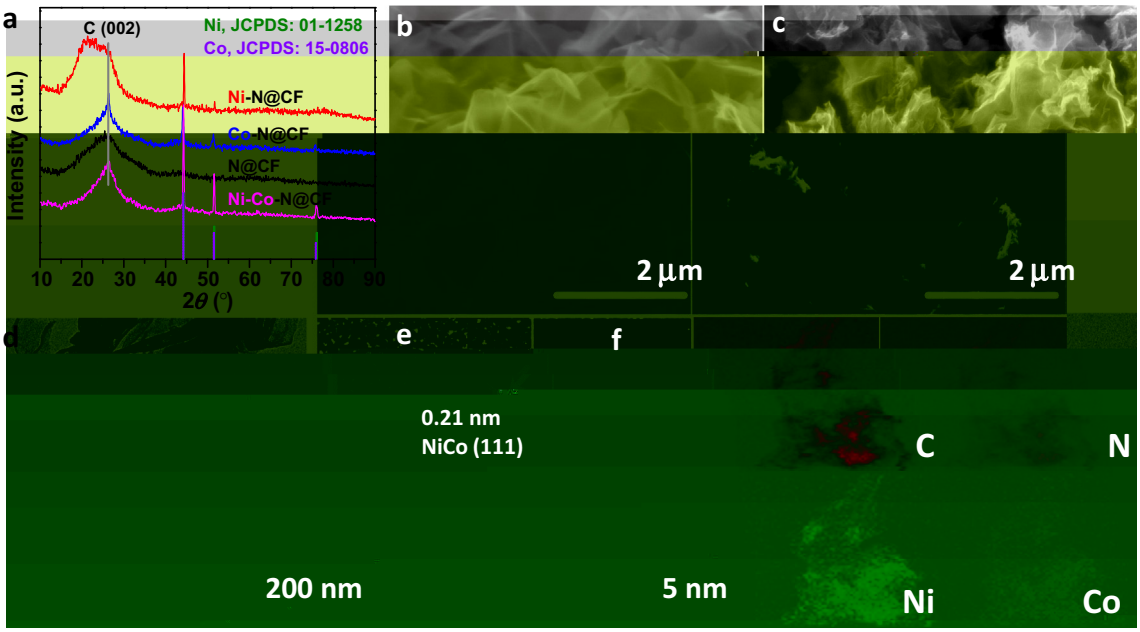

Fig. 1. (a) XRD patterns of N@CF, Ni-N@CF, Co-N@CF, and Ni-Co-N@CF. SEM images of (b) NiCo-LDH and (c) Ni-Co-N@CF. (d) TEM image, (e) high-resolution TEM image, and (f) HAADF-TEM and the corresponding EDS mappings of C, N, Ni and Co elements of Ni-Co-N@CF.

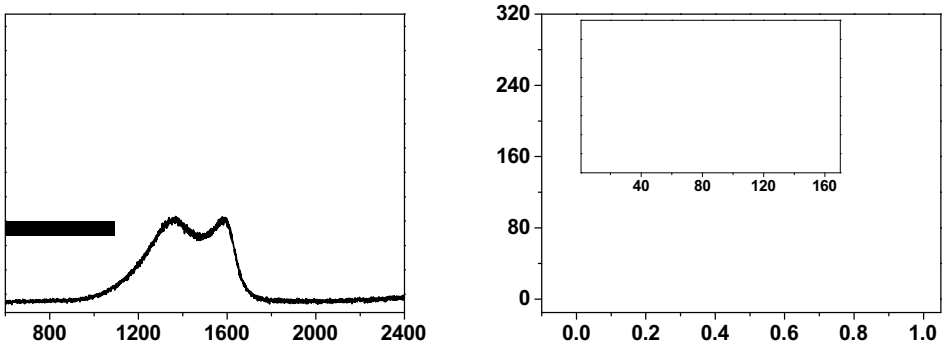

characteristic peaks, including D-band at 1350 cm^{-1} for disorder-activated edge phonon and G-band at 1580 cm^{-1} for graphitic lattice phonon [30]. The ratio of D-band to G-band (I_D/I_G) is usually utilized to evaluate a degree of disorder of the samples, wherein a smaller value of I_D/I_G indicates a higher degree of graphitization [31,32]. The structural defects of D-band in the catalysts may be caused by the -doping and/or metal influence, resulting in the loss of some graphitized carbon atoms [33,34]. As shown in Fig. 2a, the value of I_D/I_G is 1.00, 1.04, 1.02 and 0.98 for N@CF, Ni-N@CF, Co-N@CF and Ni-Co-N@CF, respectively. Interestingly, a higher graphitization degree in Ni-Co-N@CF was obtained as compare to that of Ni-Co-N@CF- (= 15 or 50) (Fig. S6a). However, the initial degree of graphitization in all the samples are very close. Moreover, the ratios of I_D/I_G decrease from 1.06 to 0.93 when the annealing temperatures increase (Fig. S6b), indicating that a higher thermal-treatment temperature could result in a higher degree of graphitization [33,35]. Numerous studies have shown that more defects are beneficial to provide more active sites, while higher graphitization helps to enhance electron transfer properties, so they cooperatively modulate ORR catalytic activity [36,37]. Therefore, it can be considered that the higher degree of graphitization is the key to the excellent ORR catalytic performance of Ni-Co-N@CF.

Nitrogen adsorption-desorption measurements were conducted to analysis the surface structural features of the prepared Ni-Co-N@CF catalyst. As shown in Fig. 2b, the Brunauer-Emmett-Teller (BET) surface area and total pore volumes of Ni-Co-N@CF are 95.9 m^2 g^{-1} and 0.33 cm^3 g^{-1}, respectively. Notably, the isotherm curves is categorized as type IV isotherm with a pronounced hysteresis loop at P/P_0 0.4–0.9 for Ni-Co-N@CF, and the average pore-size distribution of Ni-Co-N@CF by the BJH method was 13.0 nm, proving that the composite is a typical mesoporous material [38]. The mesoporous structure helps to expose more active sites and facilitates rapid gas release and electrolyte diffusion [39,40], thereby significantly enhancing ORR catalytic activity.

Inductively coupled plasma spectroscopy (ICP) tests were performed to detect the metal contents in all the samples. As shown in Table S1, the Co and Ni contents in the optimized Ni-Co-N@CF sample is about 1.07 wt% and 1.41 wt%, respectively, showing the optimal metal content compared to all other control bimetallic ORR catalysts. Moreover, the Co/Ni ratio decreases when the temperature increases. The reason may be that the Co-N species

decompose at high temperatures faster than Ni-N and leach out from the porous carbon substrate.

X-ray photoelectron spectroscopy (XPS) measurement was performed to further understand the chemical compositions as well as elemental valence of the synthesized catalysts. As shown in Fig. S7a, the survey spectrum of Ni-Co-N@CF shows clear C, O, N, Co and Ni peaks, which is consistent with the theoretical values. The high-resolution C 1s spectrum of Ni-Co-N@CF is deconvoluted into four peaks at 284.0 eV (C═C), 284.8 eV (C—C/C—N), 286.0 eV (C—O) and 288.7 eV (C═O), which are further used as the standard correction reference for other elements (Fig. S7b).

Fig. 3a shows the high-resolution Ni 2p spectra of Ni-Co-N@CF and Ni-N@CF, in which the Ni $2p_{3/2}$ region of Ni-Co-N@CF is deconvoluted into four peaks at 852.8, 854.5, 856.8 and 862.3 eV, corresponding to the metallic Ni, Ni^{2+}, Ni^{3+} and satellite peaks, respectively. It is recognized that the high-valence Ni species is mainly caused by the oxidation of air [41]. Compared with Ni-N@CF, the Ni^{2+} species in Ni-Co-N@CF material undergoes a slight negative shift (0.12 eV). In addition, the high-resolution Co 2p spectra of Ni-Co-N@CF and Co-N@CF are presented in Fig. 3b, where the Co $2p_{3/2}$ region of Ni-Co-N@CF is fitted to the metallic Co (778.5 eV), Co^{2+} (780.8 eV) and satellite peaks, respectively. It is generally believed that a portion of the Co^{2+} species coordinates with N to form Co-N active sites in the -containing composite [42]. As expected, the binding energy of Co^{2+} in Ni-Co-N@CF is a little positive shift about 0.20 eV compared to Co-N@CF, indicating that the Co species have a higher electron density than the Ni species in the composite [43]. The electronic effect between Co and Ni is related to the d-electron structure of the transition metals and the Co-N active sites [44,45]. Moreover, the high-resolution N 1s spectra of Ni-Co-N@CF as well as Ni-N@CF and Co-N@CF are discussed in Fig. 3c, where the N 1s region is mainly fitted to the pyridinic N (398.0 eV), pyrrolic N (400.2 eV), and graphitic N (403.7 eV) [46]. It is believed that the binding energy of N from the Co-N active sites is very close to the pyridinic N, thereof a higher pyridinic N content often means more active sites [47,48]. The study found that the content of pyridinic N in Ni-Co-N@CF was . 48.2%, which was slightly higher than that of N@CF modified single Ni or Co, indicating that the introduction of bimetallic Ni-Co species can increase the content of active sites, thereby leading to a higher ORR electrocatalytic activity [20].

Moreover, the elemental analyzer test showed that the nitrogen content slowly decreased as the pyrolysis temperature increased [20,49], and the doping of the bimetal contributed to the increase of the N content relative to the that of the single metal doping (Table S2). Studies have shown that higher N doping plays an important role in forming more active sites and changing the electronegativity of adjacent carbon atoms [50], which is the key to the improved electrocatalytic performance.

The electrocatalytic performance of the designed series of Ni-Co-N@CF catalysts were initially optimized by regulating the loadings of $NiCo_2O_4$ in the composites. As shown in Fig. 4a, as the theoretical contents of $NiCo_2O_4$ increase in the precursors, the half-wave potentials of Ni-Co-N@CF catalysts increased first and then decreased, whereas they had similar limiting current densities. Meanwhile, the Ni-Co-N@CF (25 mg) catalyst also showed a low H_2O_2 selectivity and nearly 4-electron electron transfer characteristics (Fig. 4b). In addition, the influence of the calcination temperatures were further optimized, and it was found that as the calcination temperatures raised, the half-wave potential and the limiting current density also increased firstly, followed by decreasing (Fig. 4c), wherein the optimized Ni-Co-N@CF (9 0 0) catalyst also showed a lower H_2O_2 selectivity and close to 4 electron-transfer numbers compared to all other catalysts (Fig. 4d). Obviously, the Ni-Co-N@CF-25 obtained by annealing the precursor at 900 °C with 25 mg $NiCo_2O_4$ showed the best ORR activity. Such high ORR performance of Ni-Co-N@CF-25 might be ascribed to the fact that the ternary Ni/Co/N doping can greatly change the electronic structure of the material, as well as the high degree of graphitization of the carbon layers [44,45]. In addition, higher calcination temperature (1000 °C and 1000 °C) may result in the loss of nitrogen (Table S2) and decrease the nitrogen-containing active sites. Therefore, Ni-Co-N@CF-25 showed the best ORR performance. If not specified, the catalyst discussed below of Ni-Co-N@CF composite was all prepared with a precursor content of $NiCo_2O_4$ for 25 mg and calcined at 900 °C in Ar atmosphere.

The electrocatalytic activities of the optimized Ni-Co-N@CF catalyst as well as N@CF, Ni-N@CF and Co-N@CF were evaluated through CV measurements in N_2- or O_2-saturated 0.1 M KOH at a

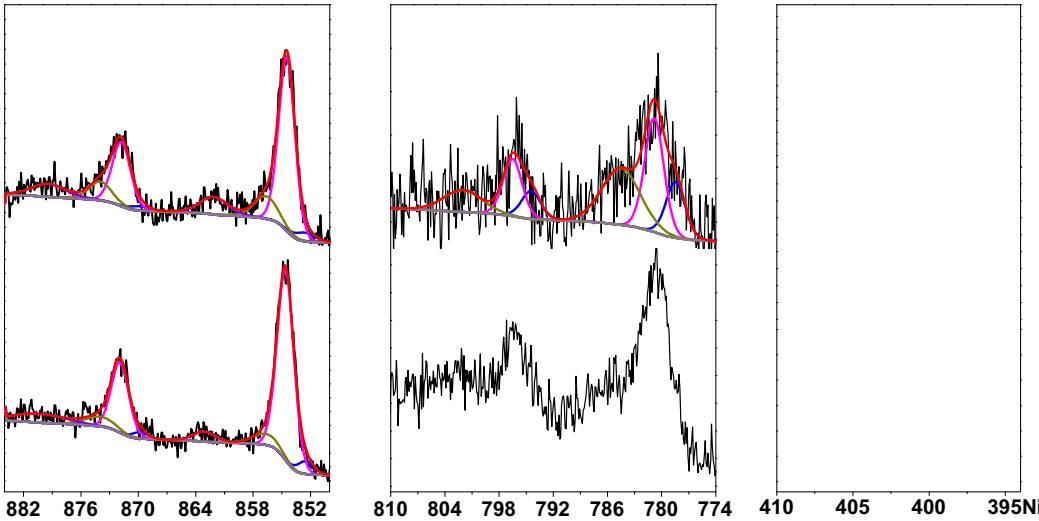

Table 1
The summarized ORR catalytic performance parameters of different catalysts in O_2-saturated 0.1 M KOH.

Catalyst	$E_{1/2}$ (V vs RHE)	J_L@0.3 V (mA cm^{-2})	H_2O_2 selectivity (%)	Electron-transfer number (n)	Tafel slope (mV dec^{-1})
Ni-Co-N@CF	0.86	4.43	10.4–15.0	3.70–3.79 (3.75)	51.0
Co-N@CF	0.85	3.84	16.4–28.1	3.44–3.67 (3.56)	35.7
Ni-N@CF	0.78	3.59	32.4–35.5	3.29–3.35 (3.32)	41.8
N@CF	0.77	4.16	6.1–22.6	3.54–-3.88 (3.71)	43.2
20 wt% Pt/C	0.87	4.82	1.2–5.4	3.78–3.79 (3.79)	55.9

the electrocatalytic activity of the synthesized catalysts for ORR in O_2-saturated KOH solution. As shown in Fig. 5b, the $E_{1/2}$ (0.86 V) and diffusion limited current density (J_L = 4.43 mA cm^{-2} at 0.3 V) of Ni-Co-N@CF catalyst were obviously higher than that of all control catalysts except that of 20 wt% Pt/C (Table 1), wherein the more positive $E_{1/2}$ and larger J_L of Ni-Co-N@CF catalyst than Ni-N@CF and Co-N@CF signified the important role of bimetallic synergy in enhancing the ORR catalytic performance. The H_2O_2 selectivity and electron transfer-number (n) calculated from RRDE tests demonstrated a nearly four-electron pathway of Ni-Co-N@CF catalyst during the ORR process where the O_2 was transformed straightforward into OH$^-$, similar to that of 20 wt% Pt/C, over a wide potential range from 0.2 to 0.75 V (Fig. 5c). The result mentioned above indicated that bimetallic co-doping could not only improve the reactivity, but also optimize the ORR selectivity of the catalyst. Tafel slope is another pivotal parameter to evaluate the electrocatalytic activity of catalysts. As showed in Fig. 5d, the Tafel slope of Ni-Co-N@CF is calculated to be 51.0 mV dec^{-1}, slightly lower than that of 20 wt% Pt/C (55.9 mV dec^{-1}), suggesting a faster ORR kinetic in alkaline medium. It should specially point out that the ORR catalytic activity of Ni-Co-N@CF is not only comprehensively superior to all control catalysts, but also much better than most of the previously reported Co-based catalysts (Table S4).

We also carried out RRDE measurements at different rotation rates varying from 400 to 2025 rpm to further determine the electron-transfer kinetics of Ni-Co-N@CF. As show in Fig. 5e, the current densities increased sharply with increasing the rotation speeds [51]. The corresponding Koutecky–Levich (K–L) plots presented in Fig. S8 showed a good linearity within the potential ranges from 0.3 V to 0.6 V, suggesting first-order reaction kinetics for ORR [52]. It can see that the electron transfer number gradually approaches 4 electrons with a gradual decrease in the selectivity of H_2O_2 as the rotation rate increases, and they are substantially constant when the rotational speed reaches 1600 rpm and above (Fig. 5f).

The electrochemical double-layer capacitances (C) of Ni-Co-N@CF and each control catalysts are firstly estimated by cyclic voltammetry in a potential window without faradaic processes, which are considered to be proportional to the electrochemically active surface area (EASA) of the catalysts. As shown in Figs. 6a and S9, we can observe that the current densities of CV curves increase regularly as the scan rates increasing from 4 to 40 mV s^{-1}. A linear correlation can be obtained through plotting each current density against the scan rate, where the C can be estimated from the slope [53,54]. As depicted in Fig. 6b, the Ni-Co-N@CF catalyst features the largest C value in KOH electrolyte (2.86 mF cm^{-2}),

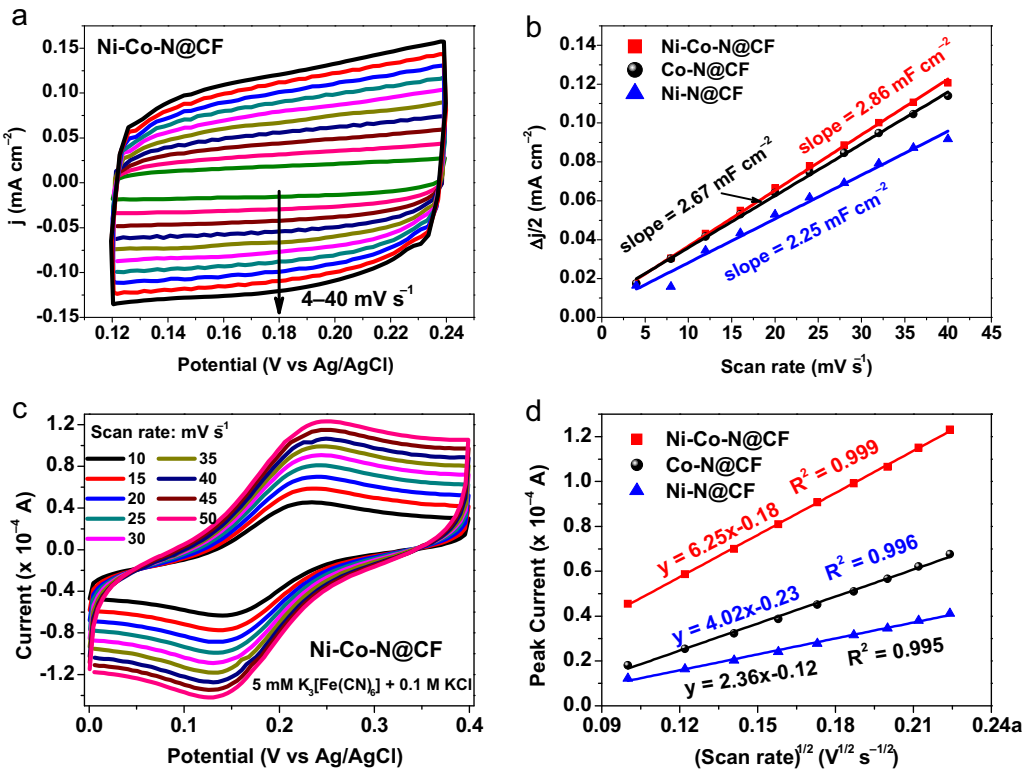

Fig. 6. (a) CV curves of Ni-Co-N@CF catalyst measured in a potential window without faradaic processes in O_2-saturated 0.1 M KOH. (b) Linear correlation of current density variation against CV scan rate in O_2-saturated 0.1 M KOH. (c) CV responses of Ni-Co-N@CF catalyst in 0.1 M KCl containing 5 mM $K_3[Fe(CN)_6]$ solution as a function of scan rate from 10 to 50 mV s^{-1}. (d) Linear dependence of peak current versus square root of san rates for Ni-Co-N@CF, Co-N@CF and Ni-N@CF, respectively.

which is 1.07- and 1.27-fold higher than that of Co-N@CF and Ni-N@CF respectively, implying a better ORR activity in alkaline solution. The higher C value of the bimetallic Ni-Co-N@CF catalyst in comparison with the single-metal counterparts further validates a synergistic effect between different components.

It is reported that a larger electrochemically active surface area (EASA) supports higher electrocatalytic activity [55,56]. Here, the EASA values of Ni-Co-N@CF, Co-N@CF and Ni-N@CF catalysts are further evaluated in 5 mM $K_3[Fe(CN)_6]$ + 0.1 M KCl solution by using Pt foil as counter electrode. The CV curves in Figs. 6c and S10 show a pair of redox peaks in which the oxidation peaks are plotted against the square root of the scan rates (Fig. 6d) and is used to calculate the EASA values by the Randles-Sevcik equation as follows [57]:

$$¼ \left(2.68 \square 10^{5}\right) \quad {}^{3/2}\upsilon^{1/2} \quad {}^{1/2} \quad {}_{0} \qquad \eth 1 \text{Þ}$$

where $_{peak}$ is the peak current, is the number of electrons involved in the reaction (n = 1, Fe^{3+} to Fe^{2+}). υ is the scan rate. A

solution. This may be ascribed to the cooperative effects among the NiCo alloy nanoparticles, -doped carbon film, and the formed Co-N species. It is known that the alloy nanoparticles can enhance the electrical conductivity (Table S3) and adjust the work function of the composite, thereby promoting the adsorption of O_2 and improving the catalytic performance [45]. To verify the role of the formed NiCo alloy nanoparticles and Co-N active sites in ORR catalysis, we designed two sets of control experiments. Firstly, the Ni-Co-N@CF was leached in 0.5 M H_2SO_4 at 90 °C for 3 h to remove the NiCo alloy nanoparticles. The XRD result showed only a peak centered at 26° corresponding to the (0 0 2) plane of graphitic carbon (Fig. S11), indicating that most of the NiCo alloy nanoparticles have been removed after acid leaching. Related LSV curves (Fig. 7e) showed that the $E_{1/2}$ of the acid leached Ni-Co-N@CF sample shifted negatively 30 mV compared with the original Ni-Co-N@CF catalyst. This result confirmed that the NiCo alloy nanoparticles are crucial for assisting the active sites to catalyze the ORR. Secondly, it is also reported that the $SCN^{\square}$ ion can poison M-N (Co-N) active sites and hinder the ORR performance of the catalysts [58]. Therefore, another contrast experiment was measured in 0.1 M KOH containing 0.01 M KSCN. The result in Fig. 7f indicated that the $E_{1/2}$ of Ni-Co-N@CF decreased by 40 mV after the addition of 0.01 M KSCN, suggesting that the Co-N species is of great importance in enhancing the ORR activity of Ni-Co-N@CF catalyst. Both the contrast experiments indicated that the Ni/Co particles and Co-N active sites are both the reasons for the excellent ORR performance.

4. Conclusion

In summary, we have reported a facile, low-cost and scalable approach of preparing ternary Ni/Co/N co-doped 2D carbon film as a highly active and durable ORR electrocatalyst in alkaline media. The hybrid catalyst with suitable amount of Ni/Co/N loading exhibits the optimized ORR electrocatalytic activity, where the half-wave potential is 0.86 V, and the limited current density is □4.43 mA $cm^{\square 2}$ at 0.3 V. Besides, the Ni-Co-N@CF shows a similar Tafel slope for ORR (51 mV $dec^{\square 1}$) as compare to Pt/C (55.9 mV $dec^{\square 1}$). The excellent ORR performance is ascribed to the synergetic effects of ternary Ni/Co/N co-doped carbon film, which not only improves the electron conductivity, but also provides more Co-N active sites. In addition, the Ni-Co-N@CF catalyst also demonstrate a highly efficient and stable properties on the stability and methanol-tolerance measurements, suggesting a great potential applications in various devices, including fuel cells, metal–air batteries, .

CRediT authorship contribution statement

Mancai Qian: Investigation and methodology. **Meijiao Xu:** Data curation. **Shuqing Zhou:** Formal analysis. **Jianniao Tian:** Supervision. **Tayirjan Taylor Isimjan:** Writing-original draft. **Zhongfeng Shi:** Supervision. **Xiulin Yang:** Writing-review & editing.

Declaration of Competing Interest

The authors declare that they have no known competing financial interests or personal relationships that could have appeared to influence the work reported in this paper.

Acknowledgements

This work has been supported by the National Natural Science Foundation of China (no. 21965005), Natural Science Foundation of Guangxi Province (2018GXNSFAA294077, 2017GXNSFGA198004), Project of High-Level Talents of Guangxi (F-KA18015, 2018ZD004) and Innovation Project of Guangxi Graduate Education (XYCSZ2019056, YCBZ2019031).

Appendix A. Supplementary material

Supplementary data to this article can be found online at https://doi.org/10.1016/j.jcis.2019.12.089.

References

[1] H. Park, S. Oh, S. Lee, S. Choi, M. Oh, Cobalt- and nitrogen-codoped porous carbon catalyst made from core–shell type hybrid metal–organic framework (ZIF-L@ZIF-67) and its efficient oxygen reduction reaction (ORR) activity, Appl. Catal., B 246 (2019) 322–329.
[2] X. Mao, G. Kour, C. Yan, Z.H. Zhu, A.J. Du, Single transition metal atom-doped graphene supported on a nickel substrate: enhanced oxygen reduction reactions modulated by electron coupling, J. Phys. Chem. C 123 (2019) 3703–3710.
[3] H. Fang, T. Huang, Y. Sun, B. Kang, D. Liang, S. Yao, J. Yu, M.M. Dinesh, S. Wu, J.Y. Lee, S. Mao, Metal-organic framework-derived core-shell-structured nitrogen-doped CoC_x/FeCo@C hybrid supported by reduced graphene oxide sheets as high performance bifunctional electrocatalysts for ORR and OER, J. Catal. 371 (2019) 185–195.
[4] X.Y. Li, L.Y. Zhang. Electrocatalysts for oxygen reduction reaction and methods of making and use thereof WO2019140678A1.
[5] Z. Miao, X. Wang, M.-C. Tsai, Q. Jin, J. Liang, F. Ma, T. Wang, S. Zheng, B.-J. Hwang, Y. Huang, S. Guo, Q. Li, Atomically dispersed Fe-N_x/C electrocatalyst boosts oxygen catalysis via a new metal-organic polymer supramolecule strategy, Adv. Energy Mater. 8 (2018) 1801226.
[6] Q. Wu, Q. Liu, Y. Zhou, Y. Sun, J. Zhao, Y. Liu, F. Liu, M. Nie, F. Ning, N. Yang, X. Jiang, X. Zhou, J. Zhong, Z. Kang, Carbon defect-induced reversible carbon-oxygen interfaces for efficient oxygen reduction, ACS Appl. Mater. Interfaces 10 (2018) 39735–39744.
[7] J. Woo, S.Y. Yang, Y.J. Sa, W.-Y. Choi, M.-H. Lee, H.-W. Lee, T.J. Shin, T.-Y. Kim, S. H. Joo, Promoting oxygen reduction reaction activity of Fe–N/C electrocatalysts by silica-coating-mediated synthesis for anion-exchange membrane fuel cells, Chem. Mater. 30 (2018) 6684–6701.
[8] Z. Lu, B. Wang, Y. Hu, W. Liu, Y. Zhao, R. Yang, Z. Li, J. Luo, B. Chi, Z. Jiang, M. Li, S. Mu, S. Liao, J. Zhang, X. Sun, An isolated zinc-cobalt atomic pair for highly active and durable oxygen reduction, Angew. Chem. Int. Ed. 58 (2019) 2622–2626.
[9] W. Hu, H. Ning, R. Nie, Z. Gong. MOFs-based NiCo@N-C bifunctional oxygen electrode catalyst and preparation method CN108722460A.
[10] B.B. Huang, Y.C. Liu, X. Huang, Z.L. Xie, Multiple heteroatom-doped few-layer carbons for the electrochemical oxygen reduction reaction, J. Mater. Chem. A 6 (2018) 22277–22286.
[11] Z.Y. Wu, W.B. Ji, B.C. Hu, H.W. Liang, X.X. Xu, Z.L. Yu, B.Y. Li, S.H. Yu, Partially oxidized Ni nanoparticles supported on Ni-N co-doped carbon nanofibers as bifunctional electrocatalysts for overall water splitting, Nano Energy 51 (2018) 286–293.
[12] W. Zhao, G. Wan, C. Peng, H. Sheng, J. Wen, H. Chen, Key single-atom electrocatalysis in metal-organic framework (MOF)-derived bifunctional catalysts, ChemSusChem 11 (2018) 3473–3479.
[13] S.L. Zhang, Y. Zhang, W.J. Jiang, X. Liu, S.L. Xu, R.J. Huo, F.Z. Zhang, J.S. Hu, Co@N-CNTs derived from triple-role CoAl-layered double hydroxide as an efficient catalyst for oxygen reduction reaction, Carbon 107 (2016) 162–170.
[14] A.K. Singh, M.W. Iqbal, V.K. Singh, M.Z. Iqbal, J.H. Lee, S.H. Chun, K. Shin, J. Eom, Molecular n-doping of chemical vapor deposition grown graphene, J. Mater. Chem. 22 (2012) 15168–15174.
[15] X. Liu, M. Antonietti, Moderating black powder chemistry for the synthesis of doped and highly porous graphene nanoplatelets and their use in electrocatalysis, Adv. Mater. 25 (2013) 6284–6290.
[16] M. Antonietti, M. Oschatz, The concept of "noble, heteroatom-doped carbons," their directed synthesis by electronic band control of carbonization, and applications in catalysis and energy materials, Adv. Mater. 30 (2018) e1706836.
[17] H. Li, Z. Zhang, T. Iyoda, M. Dou, F. Wang, Ice/salt-assisted synthesis of ultrathin two-dimensional micro/mesoporous iron and nitrogen Co-doped carbon as an efficient electrocatalyst for oxygen reduction, Chem. Eur. J. 25 (2019) 5768–5776.
[18] A.K. Naskar, M. Paranthaman, X. Yang, Y. Xia, Z.D. Hood, Y. Li. Carbon supports from waste tires for oxygen reduction catalysts US20190330440A1.
[19] I.D. Kim, G.R. Yoon, S.J. Kim, J.S. Jang, S.W. Lee, U.C. Jung, H.M. Lee. Metal oxide nanofiber functionalized on surface of heterogeneous nanoparticle catalyst, catalyst for air electrode of lithium-air battery using thereof and manufacturing method thereof KR2017107345A.
[20] L.M. Zeng, X.Z. Cui, L.S. Chen, T. Ye, W.M. Huang, R.G. Ma, X.H. Zhang, J.L. Shi, Non-noble bimetallic alloy encased in nitrogen-doped nanotubes as a highly active and durable electrocatalyst for oxygen reduction reaction, Carbon 114 (2017) 347–355.

[21] Z. Wu, P. Li, Q. Qin, Z. Li, X. Liu, N-doped graphene combined with alloys (NiCo, CoFe) and their oxides as multifunctional electrocatalysts for oxygen and hydrogen electrode reactions, Carbon 139 (2018) 35–44.

[22] M. Vukmirovic, R.R. Adzic, L. Song, Z. Liang. Electrocatalyst for the oxygen reduction reaction US20190221856A1.

[23] R. Li, Z. Hu, X. Shao, P. Cheng, S. Li, W. Yu, W. Lin, D. Yuan, Large scale synthesis of NiCo layered double hydroxides for superior asymmetric electrochemical capacitor, Sci. Rep. 6 (2016) 18737.

[24] Y. Hou, H.Y. Yuan, Z.H. Wen, S.M. Cui, X.R. Guo, Z. He, J.H. Chen, Nitrogen-doped graphene/CoNi alloy encased within bamboo-like carbon nanotube hybrids as cathode catalysts in microbial fuel cells, J. Power Sources 307 (2016) 561–568.

[25] H. Ning, G. Li, Y. Chen, K. Zhang, Z. Gong, R. Nie, W. Hu, Q. Xia, Porous N-doped carbon-encapsulated CoNi alloy nanoparticles derived from MOFs as efficient bifunctional oxygen electrocatalysts, ACS Appl. Mater. Interfaces 11 (2019) 1957–1968.

[26] L. Wang, B. Wen, X. Bai, C. Liu, H. Yang, NiCo alloy/carbon nanorods decorated with carbon nanotubes for microwave absorption, ACS Appl. Nano Mater. (2019), https://doi.org/10.1021/acsanm.1029b01842.

[27] Y. Chen, Z. Li, Y. Zhu, D. Sun, X. Liu, L. Xu, Y. Tang, Atomic Fe dispersed on N-doped carbon hollow nanospheres for high-efficiency electrocatalytic oxygen reduction, Adv. Mater. 31 (2019) e1806312.

[28] J. Sun, S.E. Lowe, L. Zhang, Y. Wang, K. Pang, Y. Wang, Y. Zhong, P. Liu, K. Zhao, Z. Tang, H. Zhao, Ultrathin nitrogen-doped holey carbon@graphene bifunctional electrocatalyst for oxygen reduction and evolution reactions in alkaline and acidic media, Angew. Chem. Int. Ed. 57 (2018) 16511–16515.

[29] J. Yan, L. Chen, X. Liang, Co_9S_8 nanowires@NiCo LDH nanosheets arrays on nickel foams towards efficient overall water splitting, Sci. Bull. 64 (2019) 158–165.

[30] J. Yang, S. Park, K.y. Choi, H.-S. Park, Y.-G. Cho, H. Ko, H.-K. Song, Activity-durability coincidence of oxygen evolution reaction in the presence of carbon corrosion: case study of $MnCo_2O_4$ spinel with carbon black, ACS Sustainable Chem. Eng. 6 (2018) 9566–9571.

[31] S. Jiang, K. Ithisuphalap, X.R. Zeng, G. Wu, H.P. Yang, 3D porous cellular $NiCoO_2$/graphene network as a durable bifunctional electrocatalyst for oxygen evolution and reduction reactions, J. Power Sources 399 (2018) 66–75.

[32] J. Yu, C. Wang, W. Yuan, Y. Shen, A. Xie, B, N Co-doped three-dimensional carbon aerogels with excellent electrochemical performance for the oxygen reduction reaction, Chem. Eur. J. 25 (2019) 2877–2883.

[33] H. Liang, D.G. Jiang, S. Wei, X.Y. Cao, T. Chen, B.B. Huo, Z. Peng, C.W. Li, J.Q. Liu, 3D cellular $CoS_{1.097}$/nitrogen doped graphene foam: a durable and self-supported bifunctional electrode for overall water splitting, J. Mater. Chem. A 6 (2018) 16235–16245.

[34] N. Wang, L. Li, D. Zhao, X. Kang, Z. Tang, S. Chen, Graphene composites with cobalt sulfide: efficient trifunctional electrocatalysts for oxygen reversible catalysis and hydrogen production in the same electrolyte, Small 13 (2017) 1701025.

[35] R. Luo, C. Liu, J. Li, C. Wang, X. Sun, J. Shen, W. Han, L. Wang, Deep-eutectic solvents derived nitrogen-doped graphitic carbon as a superior electrocatalyst for oxygen reduction, ACS Appl. Mater. Interfaces 9 (2017) 32737–32744.

[36] Z. Liang, C. Zhang, H. Yuan, W. Zhang, H. Zheng, R. Cao, PVP-assisted transformation of a metal-organic framework into Co-embedded N-enriched meso/microporous carbon materials as bifunctional electrocatalysts, Chem. Commun. 54 (2018) 7519–7522.

[37] H. Ren, Y. Wang, Y. Yang, X. Tang, Y.Q. Peng, H.Q. Peng, L. Xiao, J.T. Lu, H.D. Abruna, L. Zhuang, Fe/N/C nanotubes with atomic Fe sites: A highly active cathode catalyst for alkaline polymer electrolyte fuel cells, ACS Catal. 7 (2017) 6485–6492.

[38] Y. Wang, Y. Pan, L.K. Zhu, N.N. Guo, R.W. Wang, Z.T. Zhang, S.L. Qiu, Structure regulation of amino acids derived nitrogen doped porous carbon nanosheet through facile solid state assembly method, Micropor. Mesopor. Mat. 277 (2019) 36–44.

[39] X.X. Yang, X.L. Hu, X.L. Wang, W. Fu, X.Q. He, T. Asefa, Metal-organic framework-derived Fe_3C@NC nanohybrids as highly-efficient oxygen reduction electrocatalysts in both acidic and basic media, J. Electroanal. Chem. 823 (2018) 755–764.

[40] T. Liu, X. Zhang, T. Huang, A. Yu, Pyridinic-N-dominated carbon frameworks with porous tungsten trioxide nano-lamellae as a promising bi-functional catalyst for Li-oxygen batteries, Nanoscale 10 (2018) 15763–15770.

[41] M. Gong, Y. Li, H. Wang, Y. Liang, J.Z. Wu, J. Zhou, J. Wang, T. Regier, F. Wei, H. Dai, An advanced Ni-Fe layered double hydroxide electrocatalyst for water oxidation, J. Am. Chem. Soc. 135 (2013) 8452–8455.

[42] J. Li, S. Lu, H. Huang, D. Liu, Z. Zhuang, C. Zhong, ZIF-67 as continuous self-sacrifice template derived $NiCo_2O_4$/Co, N-CNTs nanocages as efficient bifunctional electrocatalysts for rechargeable Zn–air batteries, ACS Sustainable Chem. Eng. 6 (2018) 10021–10029.

[43] Y. Shi, Y. Zhou, D.-R. Yang, W.-X. Xu, C. Wang, F.-B. Wang, J.-J. Xu, X.-H. Xia, H.-Y. Chen, Energy level engineering of MoS_2 by transition-metal doping for accelerating hydrogen evolution reaction, J. Am. Chem. Soc. 139 (2017) 15479–15485.

[44] J.L. Long, K. Shen, L. Chen, Y.W. Li, Multimetal-MOF-derived transition metal alloy NPs embedded in an N-doped carbon matrix: highly active catalysts for hydrogenation reactions, J. Mater. Chem. A 4 (2016) 10254–10262.

[45] J. Long, R. Li, X. Gou, Well-organized Co-Ni@NC material derived from hetero-dinuclear MOFs as efficient electrocatalysts for oxygen reduction, Catal. Commun. 95 (2017) 31–35.

[46] Z. Zhang, S. Yang, H. Li, Y. Zan, X. Li, Y. Zhu, M. Dou, F. Wang, Sustainable carbonaceous materials derived from biomass as metal-free electrocatalysts, Adv. Mater. 31 (2019) e1805718.

[47] Y. Fu, H.Y. Yu, C. Jiang, T.H. Zhang, R. Zhan, X.W. Li, J.F. Li, J.H. Tian, R.Z. Yang, NiCo alloy nanoparticles decorated on N-doped carbon nanofibers as highly active and durable oxygen electrocatalyst, Adv. Funct. Mater. 28 (2018) 1705094.

[48] Q. Liu, Y. Duan, Q. Zhao, F. Pan, B. Zhang, J. Zhang, Direct synthesis of nitrogen-doped carbon nanosheets with high surface area and excellent oxygen reduction performance, Langmuir 30 (2014) 8238–8245.

[49] J.Y. Chen, H.M. Zhang, P.R. Liu, Y.B. Li, G.Y. Li, T.C. An, H.J. Zhao, Thiourea sole doping reagent approach for controllable N, S co-doping of pre-synthesized large-sized carbon nanospheres as electrocatalyst for oxygen reduction reaction, Carbon 92 (2015) 339–347.

[50] D. Guo, R. Shibuya, C. Akiba, S. Saji, T. Kondo, J. Nakamura, Active sites of nitrogen-doped carbon materials for oxygen reduction reaction clarified using model catalysts, Science 351 (2016) 361–365.

[51] X. Wu, Y. Niu, B. Feng, Y. Yu, X. Huang, C. Zhong, W. Hu, C.M. Li, Mesoporous hollow nitrogen-doped carbon nanospheres with embedded $MnFe_2O_4$/Fe hybrid nanoparticles as efficient bifunctional oxygen electrocatalysts in alkaline media, ACS Appl. Mater. Interfaces 10 (2018) 20440–20447.

[52] J. Lu, W. Zhou, L. Wang, J. Jia, Y. Ke, L. Yang, K. Zhou, X. Liu, Z. Tang, L. Li, S. Chen, Core-Shell Nanocomposites based on gold nanoparticle@zinc–iron-embedded porous carbons derived from metal-organic frameworks as efficient dual catalysts for oxygen reduction and hydrogen evolution reactions, ACS Catal. 6 (2016) 1045–1053.

[53] H. Wu, Z. Chen, Y. Wang, E. Cao, F. Xiao, S. Chen, S. Du, Y. Wu, Z. Ren, Regulating the allocation of N and P in codoped graphene via supramolecular control to remarkably boost hydrogen evolution, Energy Environ. Sci. (2019), https://doi.org/10.1039/c1039ee00555b.

[54] D. Yang, W. Hou, Y. Lu, X. Wang, W. Zhang, Y. Chen, Scalable synthesis of bimetallic phosphide decorated in carbon nanotube network as multifunctional electrocatalyst for water splitting, ACS Sustainable Chem. Eng. 7 (2019) 13031–13040.

[55] H.W. Liang, W. Wei, Z.S. Wu, X. Feng, K. Mullen, Mesoporous metal-nitrogen-doped carbon electrocatalysts for highly efficient oxygen reduction reaction, J. Am. Chem. Soc. 135 (2013) 16002–16005.

[56] H. Tan, J. Tang, J. Henzie, Y. Li, X. Xu, T. Chen, Z. Wang, J. Wang, Y. Ide, Y. Bando, Y. Yamauchi, Assembly of hollow carbon nanospheres on graphene nanosheets and creation of iron-nitrogen-doped porous carbon for oxygen reduction, ACS Nano 12 (2018) 5674–5683.

[57] R.V. Niquirilo, E. Teixeira-Neto, G.S. Buzzo, H.B. Suffredini, Formic acid oxidation at Pd, Pt and PbO_x-based catalysts and calculation of their approximate electrochemical active areas, Int. J. Electrochem. Sci. 5 (2010) 344–354.

[58] A. Samanta, C.R. Raj, Catalyst support in oxygen electrocatalysis: a case study with CoFe alloy electrocatalyst, J. Phys. Chem. C 122 (2018) 15843–15852.